POLITECNICO DI TORINO
Repository ISTITUZIONALE

The elusive half-pole in the transfer function of Peltier thermoelectric devices

(Article begins on next page)

19 April 2024

The elusive half-pole in the frequency domain transfer function of Peltier thermoelectric devices

Andrea De Marchi[1,2] and Valter Giaretto[2,3]

[1]*Dipartimento di Elettronica – Politecnico di Torino – C.so Duca degli Abruzzi, 24 – 10129 Torino, Italy*
[2]*Consorzio Nazionale Interuniversitario di Scienze fisiche della Materia (CNISM), Unità di Ricerca Politecnico di Torino C.so Duca degli Abruzzi, 24, 10129 Torino, Italy*
[3]*Dipartimento di Energetica – Politecnico di Torino – C.so Duca degli Abruzzi, 24 – 10129 Torino, Italy*

A half-pole can be expected in the transfer function of a Peltier device because proportionality between the diffusion length and the square root of the diffusion time is intrinsic in the diffusion equation. The resulting $-1/2$ bilogarithmic slope (10 dB/dec) is, however, easily masked by the thermal time constant of the load, which makes it elusive. The goal of this work is to identify the arrangements which can reveal and make usable the half-pole, because the latter can be instrumental in a servo control to increase the open-loop gain without risking instability. The diffusion equation was solved in a sine wave regime for a one-dimensional model of a Peltier device. The Laplace transform method was used, and the periodic solution was obtained using Cauchy's theorem and the method of residues. The $-1/2$ slope of the half-pole appeared observable in a frequency range which can be several decades wide, depending on details of device configuration and considered position within. Amplitude and phase of temperature and heat flux in various spots are discussed with emphasis on the physical meaning, and a comparison is provided with solutions yielded by the lumped model, which cannot show the half-pole. An experimental check of the theoretical approach and analysis was made taking into account the deviations from one-dimensionality occurring in a real Peltier device. Given a constant amplitude sine wave injected current, the quadrature component of the Seebeck voltage across the whole series of junctions was identified as the most easily measurable quantity related to the thermal response of the device. Experimental results for the latter turned out in good agreement with analytical solutions. © *2011 American Institute of Physics*. [doi:10.1063/1.3558696]

I. INTRODUCTION

While Peltier modules have long been used as cooling devices, it is only relatively recently that they are increasingly getting more common, typically in electronics and electro-optics, in the use as actuators in precision temperature control servo systems. It is likely for this reason that their frequency domain transfer function, although so crucial for a careful design of the control loop, appears to have not been studied thoroughly as yet in published work. A search through recent literature turned up only two papers[1,2] focused on the subject. Both are based on lumped equivalent circuits and, therefore, assume uniform temperature distribution in objects other than the thermoelectric components. Within the latter, temperature is assumed to vary linearly from one junction to the other. This approach underestimates the relevance of heat diffusion within the device and surrounding objects. This offers as a result an excessively simplified solution. The latter may appear reassuring as it only shows poles and zeros in the Laplace transfer function, but is unfortunately inadequate as it misses some interesting features of this unique device.

In this paper a full analysis of a Peltier thermoelectric module driven by a sine wave current is carried out by means of the heat diffusion equation. The resulting temperature sine wave is derived, in amplitude and phase, as a function of the driving frequency. It is shown that, according to the chosen spot within the structure, the (frequency domain) Bode diagram of the transfer function of the device can show a more or less wide range of frequencies within which the amplitude bilogarithmic slope is $-1/2$. This realizes what is sometimes called a half-pole in the automatic control community. This feature is unique to diffusive processes, as it stems directly from the diffusion equation, which is second order in the spatial variable but only first order in time. As a consequence, the characteristic diffusion length comes out proportional to the square root of the elapsed diffusion time, or half the period in a sine wave regime, and is, therefore, inversely proportional to the square root of the driving frequency. Previous papers seeking the transfer function of these devices missed the point because this feature is eminently elusive as it can be easily masked by thermal time constants if the thermal circuit is not specifically designed to take it up front.

This said, the 10 dB/dec slope can be particularly helpful in a servo control because it allows rapid increase of the open-loop gain below the attack frequency without the risk of instability. It is well known that the slope of the Bode diagram at the attack frequency must be smaller than 40 dB/dec in order to avoid oscillations. A slope of 30 dB/dec is considered ideal in this context, because it allows increasing the low frequency loop gain (and, therefore, the stability of the closed loop) without increasing the bandwidth of the control. The latter, in fact, may often be limited by unavoidable additional poles somewhere else in the loop. In aiming at this, the difficult part is realizing the half-pole, and this is what makes the present result attractive. The remaining 20 dB/dec necessary to turn such 10 dB/dec slope into that magic 30 dB/dec can

be easily added by introducing a lower frequency pole in the loop. Another aspect of the same result is the fact that such shallower slope of the transfer function (10 dB/dec instead of the usual 20 dB/dec of a single dominant pole) effectively extends the useful bandwidth of a Peltier module far beyond what might be expected for a thermal device, irrespective of the time constant imposed by connected thermal masses.

In the analysis reported here, the Thomson effect was neglected *a priori*, and the Joule effect was neglected in consideration of the small-signal regime in which the device would be operated in a precision loop. In fact, it is assumed here that the Peltier module be used as an actuator working around an operating point where the direct current (dc) component is low, while most of the dc needed to approach the servo control set point is provided by a different device.

The following discussion illustrates the conditions under which this simplification is acceptable. By assuming uniform Joule heat generation within the thermoelectric material and none in the electrical connections (ECs), the total heat flux in sine wave regime can be written as

$$\Phi_J = (2L_0)\frac{\rho_e j_P^2}{2}[1 - \cos(2\omega t)], \qquad (1)$$

where $\omega = 2\pi f$ is the angular frequency of the input signal, j_P is the peak current density, $2L_0$ is the length of the thermoelectric material, and ρ_e is its electrical resistivity. It is clear that the Joule effect induces both a dc contribution and one oscillating at the second harmonic of the driving frequency, which can be studied separately for the superposition principle. Neither interferes with the operation of the module at ω, unless the current is so great as to induce nonlinearity, which is not the case with the assumptions made here. Furthermore, the second is reduced by the shorter diffusion length, because it oscillates at the second harmonic. In order to judge what small-signal means in this context, the Joule flux of Eq. (1) can be compared with the peak value of the Peltier heat flux $\Phi_P = \Pi j_P$ injected at the junction, which can be done by considering the ratio between the two:

$$\frac{\Phi_J}{\Phi_P} = L_0 \frac{\rho_e}{\Pi} j_P = \frac{j_P}{j_{\lim}}. \qquad (2)$$

The quantity $j_{\lim}$ is the current density at which Peltier and Joule heat fluxes are equal, resulting in vanishing cooling of the cold side. By using typical values for relevant properties and geometry of a Peltier module, it turns out that $j_{\lim}$ is of the order of 5 A/mm^2. The current densities used in this work to run experimental tests on the theory, as well as the current levels expected in a precision temperature control, are below 0.1 A/mm^2. Therefore, the Joule effect will be neglected in the analysis.

By the same token, being the Joule effect negligible, the average temperature on the module's outer surface remains in thermal equilibrium with the environment and an adiabatic boundary working hypothesis can be adopted as a first approximation.

In the following, a one-dimensional physical model will be first introduced in Sec. II, based on which a closed form analytical solution will be found for the diffusion equation. The

physical meaning of such solution will then be discussed in Sec. III, with particular attention to the different features that the frequency domain transfer function assumes for different positions in the thermal circuit assembly. In Sec. IV, experimental results will be presented which support the analysis and confirm as a consequence the validity of the assumptions made here, at least for the small-signal operational regime.

II. PHYSICAL MODEL AND MATHEMATICAL DESCRIPTION

A one-dimensional model was considered for the Peltier thermoelectric device. The full model features five adjacent homogeneous slabs, which can be reduced to three, with the appropriate boundary conditions, by assuming symmetry about the center of the middle one. Starting from such center toward the outside of the device, the reduced model is then made of (0) a slab of p or n-doped semiconductor material (usually bismuth telluride) as thick as half of the length of the pillars, referred to in the following as PN layer, (1) a thin electrically conducting layer (usually indium brazed copper), referred to in the following as EC layer, and (2) an external electrical isolator slab (usually made of alumina ceramic), referred to in the following as EI layer.

Apart from the sign of the Peltier coefficient, no difference was assumed in the analysis between the thermoelectric properties of n-doped and p-doped semiconductors. This is not too far from reality.

Adiabatic and Dirichlet boundary conditions were respectively applied on external surface and symmetry plane, while appropriate continuity constraints were imposed at internal interfaces as detailed below with reference to Fig. 1.

Since the mathematical model consists of linear partial differential equations with constant coefficients, the Laplace transform method and the superposition principle[3,4] were used to separate oscillating and average temperature distribution fields. Solutions were found separately for the PN layer ($0 \leq x \leq L_0$) and the user side of the structure, consisting of EC ($-L_1 \leq x \leq 0$) and EI ($-L_2 - L_1 \leq x \leq -L_1$) layers. Such solutions were then matched and combined with the proper interface constraints. Because the interest here is focused on the frequency domain transfer function, only the oscillating fields were considered.

The solution was first obtained for the PN layer, by imposing a heat flux density Φ^+ injected at $x = 0$ (Fig. 1) and a constant temperature value at $x = L_0$. The resulting steady state oscillating temperature at $x = 0$ was then used as a boundary condition for the EC layer at the junction plane. With this, the solution for both EI and EC layers was obtained simultaneously, by imposing both temperature and heat flux continuity at their separation plane, at $x = -L_1$. Finally, in order to link the solution obtained for this composite layer to the one previously obtained for the semiconductor pillars, temperature continuity and heat flux balance with the Peltier flux input were also imposed at the junction between EC and PN layers at $x = 0$.

Assuming as positive the heat flux directed along the x axis in Fig. 1, and indicating with Φ the injected Peltier flux,
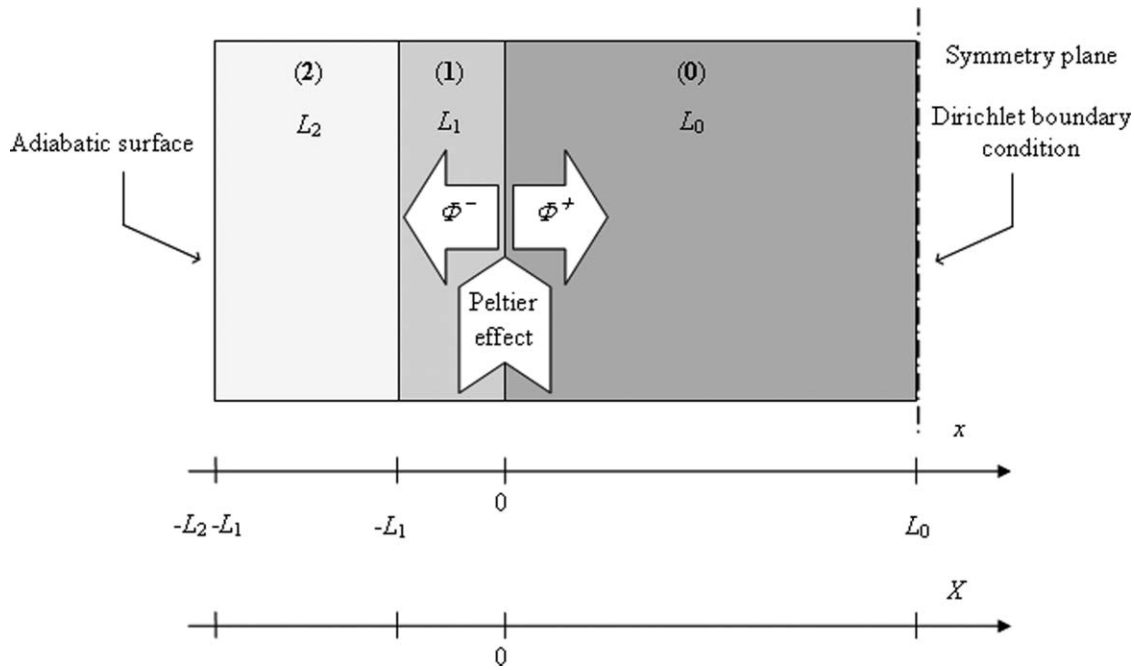
FIG. 1. Schematic diagram for a symmetric part of the thermoelectric device with the coordinate system and the thermal boundary conditions; (0) represent the half-portion of semiconductor p–n materials, (1) and (2) are the electrical connection and the external isolator layers, respectively.

such flux balance at the junction is given by $\Phi = \Phi^+ - \Phi^-$, where the minus sign appears because Φ^- points in the negative direction. Given the sine wave regime, and normalizing with respect to Φ, the balance equation can be written as

$$\sin(\omega t - \psi^+) = q^+ \sin(\omega t) - q^- \sin(\omega t - \psi^+ + \psi^-), \quad (3)$$

where ψ^+ and ψ^- are the phases at the junction of the two propagating heat fluxes with respect to the injected flux, while $q^+ = \Phi^+/\Phi$ and $q^- = \Phi^-/\Phi$ are their respective normalized amplitudes at the junction. Notice that q^- is expected to be negative coherently with the chosen sign convention. Both phases and normalized amplitudes depend on the angular frequency of the injected sine wave electrical current. Flux phases are described as in Eq. (3) in order to simplify the analysis of the PN layer, which is done first in this approach and assumes the input flux as the driving term.

Dimensionless solutions were obtained for the oscillating temperature excess field $\tilde{\vartheta}$ by following the described process and applying the condition of Eq. (3) for each driving frequency, and are discussed in the following. The temperature excess is referred to the constant temperature value at the symmetry plane at $x = L_0$.

The one-dimensional heat diffusion equation, for the oscillating part only, is then

$$\frac{\partial^2 \tilde{\vartheta}_0}{\partial x^2} - \frac{1}{\alpha_0} \frac{\partial \tilde{\vartheta}_0}{\partial t} = 0, \quad (4)$$

and the boundary conditions at $x = 0$ and $x = L_0$ are

$$-\lambda_0 \left.\frac{\partial \tilde{\vartheta}_0}{\partial x}\right|_{x=0,t} = \Pi\, j_P\, q^+ \sin(\omega t); \qquad \tilde{\vartheta}_0(L_0, t) = 0. \quad (5)$$

By introducing dimensionless variables as $X = x/L_0$ and $\tau = \omega t$, and the dimensionless oscillating temperature

$$\tilde{\Theta}_0 = \frac{\lambda_0\, \tilde{\vartheta}_0}{L_0\, \Pi\, j_P\, q^+}, \quad (6)$$

Eqs. (4) and (5) can be rewritten as

$$\frac{\partial^2 \tilde{\Theta}_0}{\partial X^2} - \Omega \frac{\partial \tilde{\Theta}_0}{\partial \tau} = 0, \quad (7)$$

with boundary conditions

$$-\left.\frac{\partial \tilde{\Theta}_0}{\partial X}\right|_{X=0,\tau} = \sin\tau, \quad \tilde{\Theta}_0(1, \tau) = 0. \quad (8)$$

In the following, the dimensionless quantity $\Omega = \omega/\omega_0$ will be referred to as the relative frequency, where $\omega_0 = \alpha_0/L_0^2$ is the angular frequency at which the thermal diffusion length in the PN layer is equal to $\sqrt{2}L_0$. The steady state solution of Eq. (7) with boundary conditions (8) can be obtained from the Laplace transform in its variable p, which is

$$\bar{\Theta}_0(X, p) = \frac{\sinh\left[(1 - X)\sqrt{\Omega p}\,\right]}{\sqrt{\Omega p}(1 + p^2)\, \cosh\left(\sqrt{\Omega p}\,\right)}. \quad (9)$$

In Eq. (9), conjugate poles at $p = \pm i$ indicate that the solution is sinusoidal at the driving frequency. The infinite number of poles on the imaginary axis, implicit in the hyperbolic function in the denominator, is instead related to the transient behavior and their role will not be discussed further. The steady state periodic solution obtained by Cauchy's theorem and the method of residues at the mentioned simple poles is then

$$\tilde{\Theta}_0(X, \tau) = A_0(X, \Omega)\cos\tau + B_0(X, \Omega)\sin\tau \quad \forall\, 0 \leq X \leq 1, \quad (10)$$

where coefficients $A_0(X, \Omega)$, $B_0(X, \Omega)$ are defined in the Appendix.

Turning now to the EC and EI layers, the dimensionless heat diffusion equation (7) is obviously still valid, provided Ω is substituted by Ω/κ_1 and Ω/κ_2, respectively, in the two layers, where $\kappa_1 = \alpha_1/\alpha_0$ and $\kappa_2 = \alpha_2/\alpha_0$ are the local relative thermal diffusivities.

Dimensionless interface positions are $X_1 = L_1/L_0$ and $X_2 = (L_1 + L_2)/L_0$, and dimensionless oscillating temperatures $\hat{\Theta}_1$ and $\hat{\Theta}_2$ in the two regions are defined as in Eq. (6), based on the local real oscillating temperatures $\hat{\vartheta}_1$ and $\hat{\vartheta}_2$.

The diffusion equation was solved for the two layers with the boundary conditions

$$\left.\frac{\partial \tilde{\Theta}_2}{\partial X}\right|_{X=-X_2} = 0, \tag{11}$$

$$\tilde{\Theta}_1(0, \tau) = \tilde{\Theta}_0(0, \tau), \tag{12}$$

and the imposition of temperature and heat flux continuity at $X = -X_1$

$$\tilde{\Theta}_1(-X_1, \tau) = \tilde{\Theta}_2(-X_1, \tau); \quad \left.\frac{\partial \tilde{\Theta}_1}{\partial X}\right|_{X=-X_1}$$

$$= \frac{\Lambda_2}{\Lambda_1} \left.\frac{\partial \tilde{\Theta}_2}{\partial X}\right|_{X=-X_1}, \tag{13}$$

where $\Lambda_1 = \lambda_1/\lambda_0$ and $\Lambda_2 = \lambda_2/\lambda_0$ are the relative thermal conductivities of EC and EI layers.

By following the same method as above to solve the diffusion equations, the Laplace transforms $\bar{\Theta}_1$ and $\bar{\Theta}_2$ of dimensionless temperatures in the two layers were found, and are here reported:

$$\bar{\Theta}_1(X, p) = \left[A_0(0, \Omega)\frac{p}{1 + p^2} + B_0(0, \Omega)\frac{1}{1 + p^2} \right]$$

$$\times \frac{\cosh\left[(X_2 - X_1)\sqrt{\frac{\Omega}{\kappa_2}p}\right]\cosh\left[(X_1 + X)\sqrt{\frac{\Omega}{\kappa_1}p}\right] + \frac{E_2}{E_1}\sinh\left[(X_2 - X_1)\sqrt{\frac{\Omega}{\kappa_2}p}\right]\sinh\left[(X_1 + X)\sqrt{\frac{\Omega}{\kappa_1}p}\right]}{\cosh\left[(X_2 - X_1)\sqrt{\frac{\Omega}{\kappa_2}p}\right]\cosh\left(X_1\sqrt{\frac{\Omega}{\kappa_1}p}\right) + \frac{E_2}{E_1}\sinh\left[(X_2 - X_1)\sqrt{\frac{\Omega}{\kappa_2}p}\right]\sinh\left(X_1\sqrt{\frac{\Omega}{\kappa_1}p}\right)} \tag{14}$$

$$\bar{\Theta}_2(X, p) = \left[A_0(0,)\frac{p}{1 + p^2} + B_0(0, \Omega)\frac{1}{1 + p^2} \right]$$

$$\times \frac{\cosh\left[(X_2 + X)\sqrt{\frac{\Omega}{\kappa_2}p}\right]}{\cosh\left[(X_2 - X_1)\sqrt{\frac{\Omega}{\kappa_2}p}\right]\cosh\left(X_1\sqrt{\frac{\Omega}{\kappa_2}p}\right) + \frac{E_2}{E_1}\sinh\left[(X_2 - X_1)\sqrt{\frac{\Omega}{\kappa_2}p}\right]\sinh\left(X_1\sqrt{\frac{\Omega}{\kappa_2}p}\right)}, \tag{15}$$

where $E_1 = e_1/e_0$ and $E_2 = e_2/e_0$ are the relative thermal effusivities of EC and EI layers. Similar to Eq. (10), the time domain solutions obtained from Eqs. (14) and (15) by the method of residues in the respective X ranges turn out to be

$$\tilde{\Theta}_i(X, \tau) = A_i(X, \Omega)\cos\tau + B_i(X, \Omega)\sin\tau, \tag{16}$$

where $A_i(X, \Omega)$ and $B_i(X, \Omega)$ are defined in the Appendix for $i = 1, 2$.

The obtained solutions need at this point to be balanced according to Eq. (3). In order to do that, the outgoing heat flux $\Phi^- = q^-\sin(\tau - \psi^+ + \psi^-)$ must be calculated. For the EC layer ($i = 1$) it is found from Eq. (16) that

$$\frac{\Phi^-}{q^+} = -\Lambda_1 \left.\frac{\partial \tilde{\Theta}_1(X, \tau)}{\partial X}\right|_{X=0}$$

$$= -\Lambda_1\left[A_1'(0, \Omega)\cos\tau + B_1'(0, \Omega)\sin\tau\right], \tag{17}$$

where $A_1'(0, \Omega)$ and $B_1'(0, \Omega)$ are defined in the Appendix.

The quantities q^+ and ψ^+ can then be found by splitting Eq. (3) in two equations for the components in phase and in quadrature with $\sin\tau$, obtaining

$$q^+ = \left[\sqrt{\left[\Lambda_1 A_1'(0, \Omega)\right]^2 + \left[1 + \Lambda_1 B_1'(0, \Omega)\right]^2}\right]^{-1},$$

$$\psi^+ = -\tan^{-1}\left[\frac{\Lambda_1 A_1'(0, \Omega)}{1 + \Lambda_1 B_1'(0, \Omega)}\right]. \tag{18}$$

By feeding these quantities back in Eq. (3), the quantities $q-$ and ψ can now be found by splitting again Eq. (3) in two equations for the components in phase and in quadrature with $\sin(\tau - \phi)$ obtaining, in accordance with the previously discussed sign convention,

$$q^- = -\sqrt{[q^+\sin\psi^+]^2 + [1 - q^+\cos\psi^+]^2},$$

$$\psi^- = \tan^{-1}\left[\frac{q^+\sin\psi^+}{1 - q^+\cos\psi^+}\right]. \tag{19}$$

At this point the fluxes have been balanced at the junction, and the dimensionless temperatures can be calculated at different positions within the Peltier module. In order to do that, it is convenient to refer all phases to that of the input current because it is experimentally available, contrary to the phase of heat flux Φ^+. Introducing then $\hat{\tau} = \tau - \psi^+$ as the
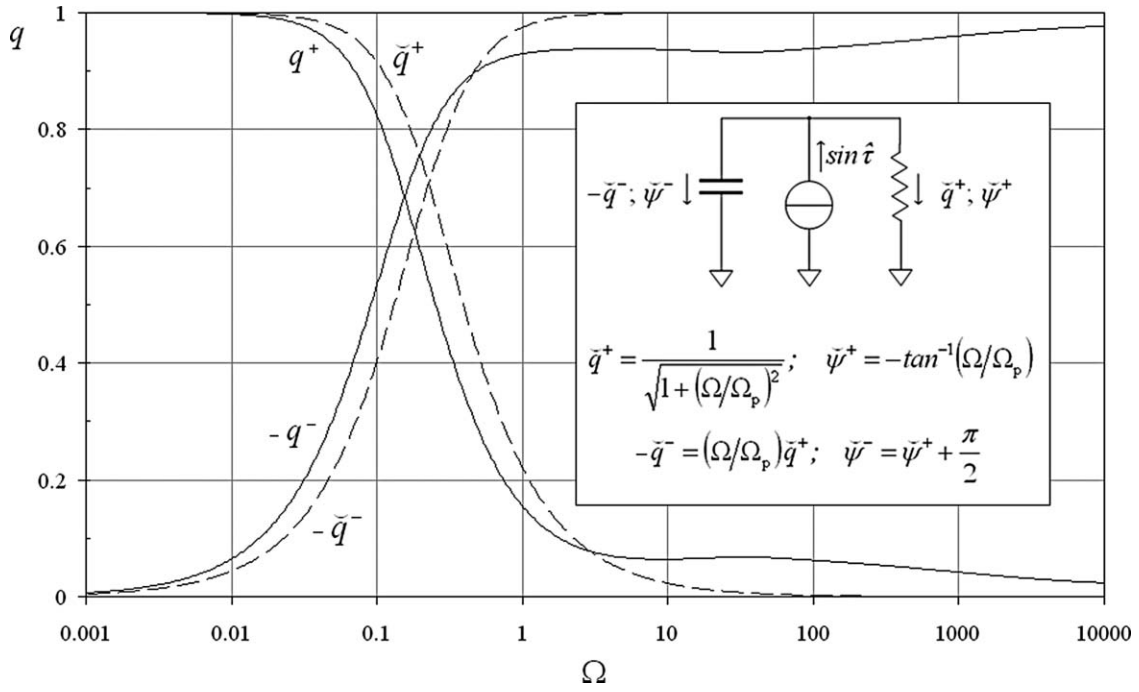
FIG. 2. Relative peak amplitude vs relative frequency of both inward and outward heat fluxes defined in Eqs. (18) and (19) (solid line) and their approximation by Eq. (22) (dashed line) obtained with the shown lumped parameters model.

new dimensionless time variable, the dimensionless temperatures in the respective X ranges within the three layers ($i = 0$, 1, 2) are

$$\hat{\Theta}_i(X, \hat{\tau}) = \frac{\lambda_0 \tilde{\vartheta}_i}{L_0 \Pi j_p} = q^+[A_i(X, \Omega)\cos(\hat{\tau} + \psi^+)$$
$$+ B_i(X, \Omega)\sin(\hat{\tau} + \psi^+)]$$
$$= \hat{A}_i(X, \Omega)\cos\hat{\tau} + \hat{B}_i(X, \Omega)\sin\hat{\tau}, \qquad (20)$$

where $\hat{A}_i(X, \Omega)$ and $\hat{B}_i(X, \Omega)$ are detailed in the Appendix.

Finally, peak amplitudes and phases of the dimensionless temperatures are easily obtained at the specified positions:

$$^P\hat{\Theta}_i(X_i, \Omega) = \sqrt{\hat{A}_i(X_i, \Omega)^2 + \hat{B}_1(X_i, \Omega)^2},$$

$$\varphi_i(X_i, \Omega) = \tan^{-1}\left[\frac{\hat{A}_i(X_i, \Omega)}{\hat{B}_i(X_i, \Omega)}\right], \qquad (21)$$

where X_i represents in turn for $i = 0$, 1, 2 the coordinates 0, $-X_1$, and $-X_2$ of the layer interfaces.

In the next paragraph the frequency domain behavior of heat fluxes shown in Eqs. (18) and (19) and temperatures obtained from Eq. (21) will be discussed.

III. DISCUSSION OF ANALYTICAL SOLUTIONS

In order to discuss analytical solutions with the help of suitable plots, assumptions were made on geometry and thermophysical properties of involved materials. In particular, values were chosen which are reasonably close to those of commonly available modules. These are: $X_1 = 0.1$ and $X_2 = 0.5$ for the geometry, and $\Lambda_1 = 400$; $\Lambda_2 = 10$; $\kappa_1 = 100$ and $\kappa_2 = 1$ for the relative properties of EC and EI layers.

It is convenient to first discuss how the Peltier heat flux injected at the junction ($X = 0$) is divided in two fractions flowing inward and outward, respectively.

Relative amplitudes and phases of such fluxes are described by Eqs. (18) and (19) and shown in Figs. 2 and 3 as a function of the relative frequency Ω. A comparison with the lumped equivalent circuit solutions (dashed lines) is also provided in these figures. At low frequencies the full calculation appears to be well approximated by the lumped model solutions, written as

$$q^+ \approx \breve{q}^+ = \sin\psi^-; \qquad -q^- \approx -\breve{q}^- = \cos\psi^-. \qquad (22)$$

As expected, it appears that the two fluxes are in quadrature for low frequencies, starting at $\Omega = 0$ with the Peltier injected flux flowing totally inward to yield the temperature difference across the conductance of the PN layer, and with the outward flux gradually growing for increasing frequencies to fill the thermal capacitance of the EI layer, so that temperature continuity be guaranteed at the junction.

At the relative angular frequency Ωp of the thermal pole, the two fluxes are still close to being in quadrature, phased as expected about $\pi/4$ either side of the Peltier injected flux, in good agreement with the electrical analogy of a resistance (PN layer) in parallel with a capacitance (EC and EI layers). For the position of this thermal pole, a good estimate is easily found from the values of such resistance and capacitance, and can be written as

$$\Omega_p \cong \left[\frac{\Lambda_1}{\kappa_1}X_1 + \frac{\Lambda_2}{\kappa_2}(X_2 - X_1)\right]^{-1}. \qquad (23)$$

At higher frequencies the flux is increasingly driven predominantly into the external EI layer as its thermal
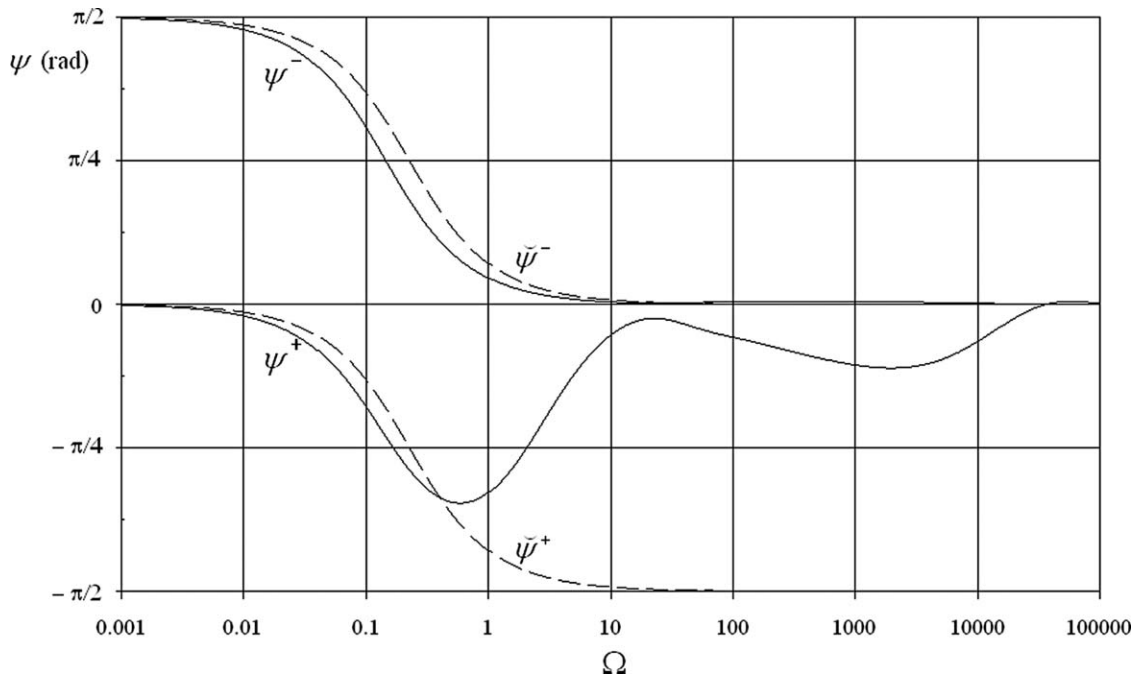
FIG. 3. Phase vs relative frequency for heat fluxes defined in Eqs. (18) and (19) (solid line) and their approximation shown in Fig. 3 (dashed line).

impedance gradually decreases due to its capacitive behavior, and the phase of this outward flux tends to zero as predicted by the simple electrical analogy. In this range, the amplitude q^+ of the inward flux does indeed decrease correspondingly according to Eq. (22), but its phase ψ^+ soon deviates from the simplified model above Ω_p, clearly indicating that at higher frequencies such lumped model is no longer adequate. Eventually, both fluxes will carry heat into thermally thick layers and will, therefore, be both aligned in phase with Peltier injected flux.

In Fig. 3 the lower solid curves show the real behavior of ψ^+ and ψ^-, the dashed lines refer to the simplified lumped model in which the fluxes flowing into capacitance and thermal resistance are expected to be always in quadrature. At even higher frequencies Fig. 3 shows again a bump in the behavior of ψ^+. This effect is related to the presence of the EC layer; in fact, it disappears if the thickness of the latter is forced to vanish in the model.

In Figs. 4 and 5, peak amplitude and phase of resulting dimensionless temperatures calculated at $X = 0$, $X = -X_1$, and $X = -X_2$ according to Eq. (21) are shown as a function of the relative frequency Ω.

In particular, it is worth discussing the asymptotic behavior of $^P\hat{\Theta}_0$ at $X = 0$ for high frequencies, as it highlights the role played by the different layers. In fact, for $\Omega \to \infty$ Eq. (21) with $i = 0$ is well approximated by

$$^P\hat{\Theta}_0(0, \Omega) \approx \frac{1}{\sqrt{\Omega}} \cdot \frac{1}{1 + E_1}, \tag{24}$$

where $E_1 = e_1/e_0$ is the relative effusivity of the EC layer with respect to the PN layer, shown in Fig. 4 by the dashed straight line a. This asymptote is approached when the frequency is so high that the thermal diffusion length in the EC layer is shorter than its thickness. It is interesting to point out

that such asymptote moves to the position b, also shown in the figure, if the thickness of the EC layer is forced to vanish in the model. In fact, the layer directly facing the junction is in this case the EI layer, and Eq. (24) must be rewritten with $E_2 = e_2/e_0$ instead of E_1.

Starting from low frequencies, after the extinction of the thermal pole effect, the $^P\hat{\Theta}_0$ curve tries first to reach the b asymptote as the diffusion length in the EI layer becomes shorter than its thickness, but is eventually attracted by the a asymptote when the same happens in the EC layer. In fact, by reducing the thickness of the EC layer by factor of 3 in the model, without changing the thickness of the EI layer, this transition is moved to higher frequencies and the b asymptote can be approached more closely before the effect of the EC layer is felt (dotted line in Fig. 4). The opposite happens if the EC layer is made thicker.

In Fig. 5 it can be seen that φ_0 approaches $-\pi/2$ at relative frequencies slightly higher than 1, where the amplitude $^P\hat{\Theta}_0$ follows the asymptote c sloping as $1/\Omega$ called for by the thermal pole. This happens because in this frequency range the injected flux flows mainly into the capacitive EI layer, as shown in Fig. 2. At higher frequencies, φ_0 turns back up toward $-\pi/4$ as the EI layer becomes thermally thick. It is interesting to point out that here too, as for ψ^+, the high frequency bump observed in the phase φ_0 disappears if the EC layer is removed, clearly showing that it is produced by its presence. At even higher frequencies, such phase eventually settles asymptotically on $-\pi/4$ as expected for a semi-infinite slab.

In Fig. 4, peak temperatures $^P\hat{\Theta}_1$ and $^P\hat{\Theta}_2$ at positions $-X_1$ and $-X_2$ are also shown as a function of frequency. It can be noticed that $^P\hat{\Theta}_1$ follows closely $^P\hat{\Theta}_0$ until the EC layer turns thermally thick. A thicker EC layer would move such deviation to lower frequencies. In fact, for any position on the
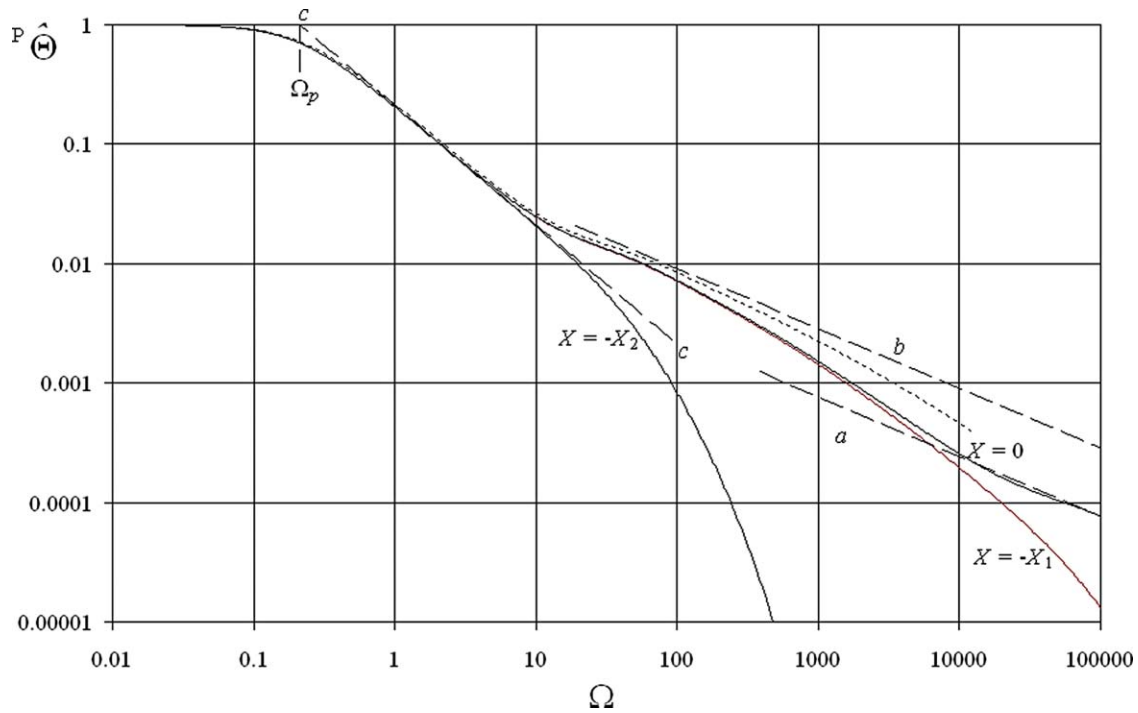
FIG. 4. Dimensionless peak amplitude of the oscillating temperatures vs relative frequency (solid lines) calculated at the main interface positions $X = 0$, $X = -X_1$, and $X = -X_2$. Ω_p is the relative frequency of the thermal pole. Asymptotic trends a, b, and c are called for by the EC layer, the EI layer, and the thermal pole, respectively. The dotted curve represents the peak amplitude at the junction ($X = 0$) obtained by reducing the thickness of the EC layer.

user side of the device ($-X_2 \leq X \leq 0$) a relative knee frequency $\Omega_{k,X}$ exists at which the local temperature starts to fall quickly for that reason. This happens, for example, in the EC layer when the diffusion length becomes shorter than $\sqrt{2}L_1$. This is very relevant if one intends to use the Peltier device as a transducer in a servo control loop, because the rapid amplitude decrease and the dramatic phase rotation occurring in

its transfer function beyond Ω_k make it unusable in that frequency range.

In Fig. 6, a much thicker EI layer is assumed ($X_2 \approx -6$) with the result of moving the thermal pole to a much lower frequency, uncovering in this way a behavior of $^P\hat{\Theta}_0$ which follows the $-1/2$ sloped trend of asymptote b down to where the latter reaches 1, at the relative corner frequency Ω_c
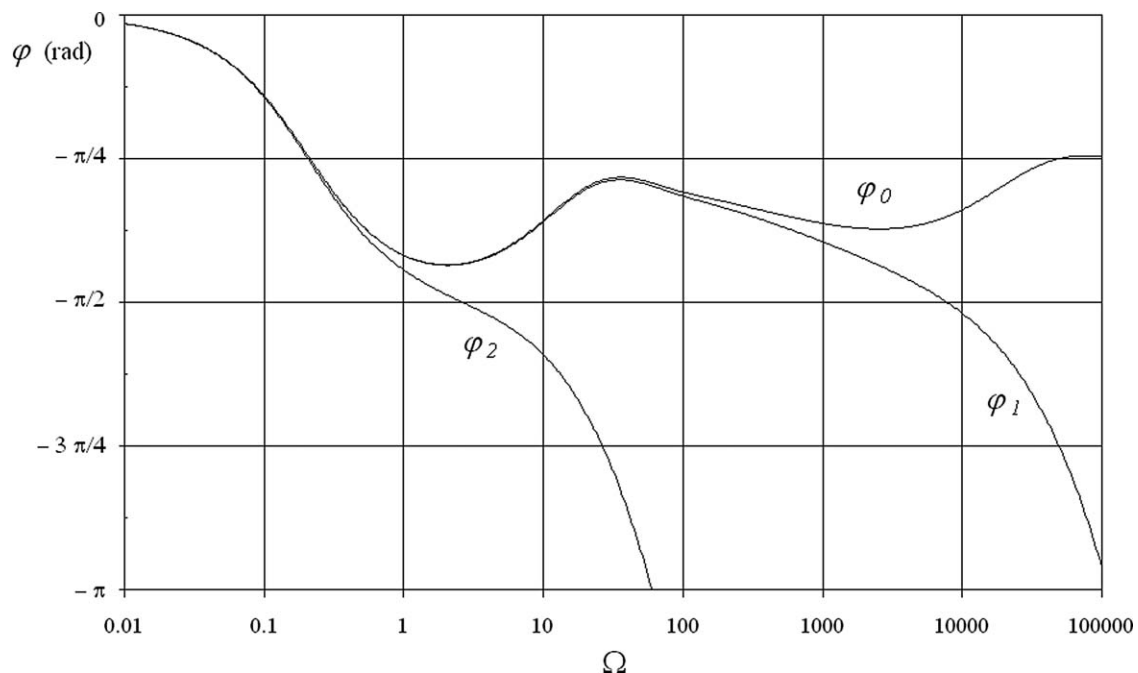

FIG. 5. Phases for temperature vs relative frequency calculated at the main interface positions $X = 0$, $X = -X_1$, and $X = -X_2$.
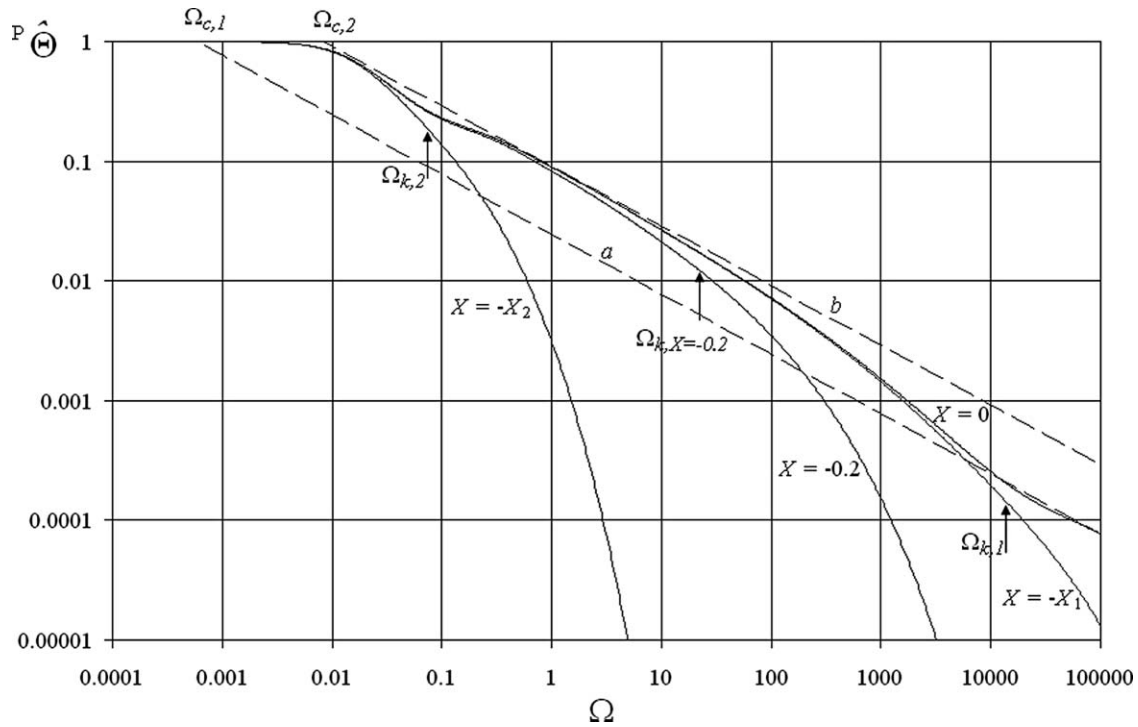
FIG. 6. Dimensionless peak amplitude of the oscillating temperatures vs relative frequency expected for a thicker EI layer (solid lines) calculated at the main interface positions $X = 0$, $X = -X_1$, $X = -X_2$, and at the random pick $X = -0.2$, with their relative knee frequencies Ω_k. Relative corner frequencies Ω_c are shown for asymptotes a and b.

given by

$$\Omega_c = (1 + E_2)^{-2}. \tag{25}$$

Also shown in Fig. 6 are the dimensionless temperature curves at positions $X = -X_1$, $X = -X_2$, and $X = -0.2$ (a random pick), together with their respective relative knee frequencies $\Omega_{k,1}$, $\Omega_{k,2}$, and $\Omega_{k,X} = -0.2$. The range over which this magic slope of $-1/2$ occurs at location X is given by $\Omega_{K,X}/\Omega_C$ and can be seen in Fig. 6 for chosen values of X. In a case in which both layers were made of the material hereto assumed for the EC layer, such range would be about seven decades.

IV. EXPERIMENTAL VALIDATION

In order to run an experimental check of the exposed analysis, adaptations must be first introduced in the model to take into account deviations from one-dimensionality occurring in the real device.

To this aim, constriction and spreading resistances are introduced to account for heat flows from one region to another of different cross sectional area. In fact, depending on the geometry of the considered Peltier device, area filling factors can be defined as the ratio between the cross sectional areas of adjacent materials at their interface. Filling factor ξ_{0-1} is then given by the ratio between the cumulative cross section of semiconductor pillars and that of the electrical interconnections. Similarly, ξ_{1-2} is the ratio between the latter and the area of the external face of the module.

Extensive literature about constriction and spreading resistances is available for electronic devices operating in dc

conditions. A simplified model of suitable geometry usable for the analysis of available devices was proposed by Lee et al.[5] The model considers, with various boundary conditions, the thermal coupling between a source pillar and a centered plate of finite dimensions. In addition to the area filling factor ξ, the ratio between thickness and width of the plate is needed to fully describe the geometry. To this aim the aspect ratio ζ given by the plate thickness divided by the square root of its surface area is used here. The spreading resistance obtained with this approach was added to the intrinsic resistance of the plate through an alteration of its material thermal conductivity by means of the coefficient β defined below.

In the case of a Peltier module, the constriction and spreading resistance model must be applied twice with different boundary conditions: once for the interface between the semiconductor pillar and the electrical interconnection, and once for the interface between the latter and the external insulator. An isothermal boundary was assumed for the analysis of the first interface, and adiabatic conditions were imposed in the second. This assumption was, however, adopted for simplicity and no inquiry was tried on its validity. Two different values ζ_1 and ζ_2 were used for the two plates.

The equivalent relative thermal conductivities Λ_1 and Λ_2 can then be written as[5]

$$\Lambda_1 = \beta_1 \frac{\lambda_1}{\lambda_0};$$

$$\beta_1 = \left\{ 1 + \frac{(1 - \sqrt{\xi_{0-1}})^{3/2}}{2\zeta_1 \sqrt{\xi_{0-1}}} \tanh\left[\zeta_1 \left(\pi^{3/2} + \frac{1}{\sqrt{\xi_{0-1}}} \right) \right] \right\}^{-1}, \tag{26}$$

$$\Lambda_2 = \beta_2 \frac{\lambda_2}{\lambda_0};$$

$$\beta_2 = \left\{ 1 + \frac{(1 - \sqrt{\xi_{1-2}})^{3/2}}{2\zeta_2 \sqrt{\xi_{1-2}} \tanh\left[\zeta_2 \left(\pi^{3/2} + \frac{1}{\sqrt{\xi_{1-2}}}\right)\right]} \right\}^{-1}.$$

$$(27)$$

By the same token, the volumetric heat capacity of the plate materials must also be altered, with a division by the filling factor, to account for the varying cross sections. The relative thermal diffusivities of the two materials will then be calculated as follows:

$$\kappa_1 = \beta_1 \xi_{0-1} \frac{\alpha_1}{\alpha_0}, \quad \kappa_2 = \beta_2 \xi_{1-2} \frac{\alpha_2}{\alpha_0}. \quad (28)$$

As for the experimental approach, the Seebeck voltage V_ε developed across the whole series of junctions and appearing at the leads of the Peltier module was identified as the quantity most easily measurable and accurately related with the thermal response of the device to the injected current, and was, therefore, used to support the validity of the calculated behavior of the junction temperature ϑ_0.

In fact, such voltage is given by $V_\varepsilon = 2\, n\vartheta_0\, \varepsilon$, where n is the total number of semiconductor pillars, ε is the junction's Seebeck coefficient, and ϑ_0 is the actual temperature at the very spot $X = 0$ considered in the analysis. For the Peltier device used to validate the analysis, for which $n = 34$ and $\varepsilon \approx 200\, \mu V/K$, the module's Seebeck coefficient amounts to about 14 mV/K, which means that measurement sensitivities of a few tenth of a mK are relatively easy to reach with this approach. This in turn means that a temperature dynamic range of four decades can be explored in measuring the transfer function without exceeding the limit of 1 K differential temperature, which allows us to keep the injected current on the order of 1% of the current limit of the device. The assumption adopted in the analysis that the Joule effect can be neglected is then well justified.

The only real hurdle faced in measuring the Seebeck voltage is the need to accurately discriminate it from the Ohmic voltage drop on which it sits. This is a nontrivial operation which in principle requires accurate modeling of the electrical series resistance. While it would be probably feasible, with adequate effort, to reach the percent level in this way, it would be certainly cumbersome.

The approach taken here was to measure the amplitude of the sole quadrature component of V_ε, in the assumption that reactive parasitic parameters of the module's impedance can be neglected. The latter do in fact introduce a non-Seebeck contribution to the quadrature voltage. As it turns out, in the used device, the quadrature voltage due to the module's parasitic inductance starts to overwhelm the Seebeck signal only above 50 Hz. This paves the road to a much more accurate and easier measurement, which also has the additional advantage of enabling a combined test of both amplitude and phase of the calculated junction temperature.

More promising measurement strategies can certainly be devised for the implementation of this approach, including compensation of the parasitic inductance, narrow band
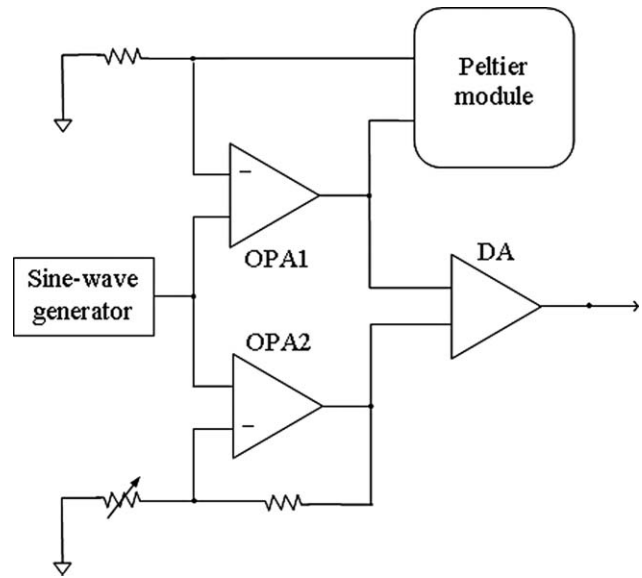

FIG. 7. Schematics of the electronic measurement circuit. Low noise OP177 operational amplifiers are used for the OPAs. The DA was an AD621 configured for a gain of 100 and white input voltage noise density of 10 nV/$\sqrt{\text{Hz}}$.

filtering to improve the signal-to-noise ratio, and above all the use of better calibrated instrumentation. However, in the absence of accurate information on the physical characteristics of the device under test, in particular on geometry and thermophysical properties of materials, the quick-and-dirty solution shown in Fig. 7 was found adequate for the desired support to the analysis and was, therefore, adopted in the present work.

In fact, the total type B uncertainty produced by the chosen instrumentation turned out to be negligible with respect to type B uncertainties imposed on analytical results by the scarcity of available information. The comparison type B uncertainty is, therefore, dominated by the latter, which suggests that it is not worth the effort to improve the measurement system at this level of *a priori* knowledge on the device under test.

As shown in Fig. 7, the input sine wave voltage signal forces a proportional current through the Peltier device with the assistance of the operational amplifier OPA1, while it is also separately processed with the help of OPA2 and the following variable attenuator to produce a signal that matches the in-phase component of the voltage appearing at the output of OPA1. The latter consists of the input voltage, plus the Ohmic drop across the module, plus the in-phase component of the Seebeck voltage. The differential amplifier (DA) takes the difference between these two signals and amplifies it as needed. At each driving frequency, the variable attenuator is adjusted to reduce the differential output to the quadrature component before its amplitude is measured. Low noise, low offset, and low drift amplifiers were used in the setup in order to optimize stability and signal-to-noise ratio, which made measurements precise and easy to perform. In particular, the OP177 and the AD621 models were chosen for operational amplifiers and differential amplifier, respectively. In the absence of bandwidth reduction, the resulting total rms voltage noise at the output of the 40 dB gain DA turned out to be 0.3
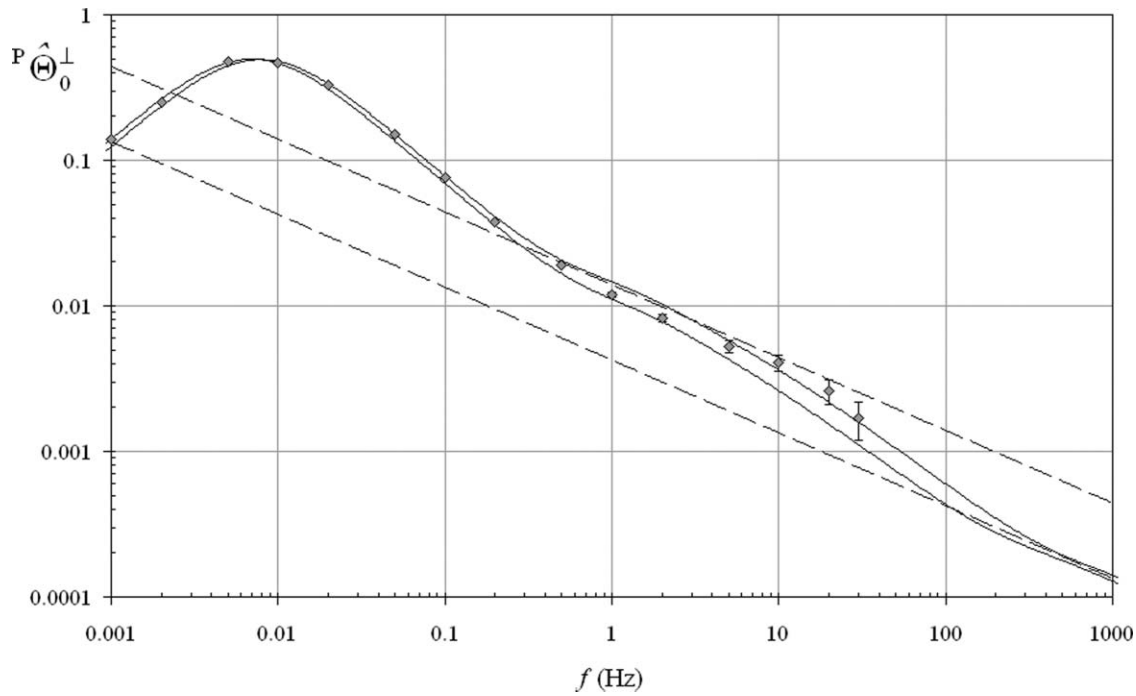
FIG. 8. Comparison between experimental and analytical results for the quadrature component of the dimensionless peak temperature. Uncertainties are 1σ. Bars around data are type A only. The model dominated type B uncertainty is indicated by the band between the two curves, which, however, includes no contribution from the adopted constriction and spreading resistance model. Dashed lines are reported for slope reference only ($-1/2$).

mV_{rms}, which is consistent with typical data sheet values for the adopted devices.

Both operations of isolating and measuring the quadrature component of the Seebeck voltage were performed with an oscilloscope. The Lissajous method[6] was used to find the quadrature, and the instrument's calibration of vertical scales was relied on for amplitude measurements, for the reasons detailed above.

In Fig. 8, experimental results are presented for the quadrature component of the Seebeck voltage, obtained with the outlined method. Data points are shown with the associated type A uncertainty introduced by instrumentation noise. Clearly, the latter becomes relevant only for the higher frequency points, where signals are small. It may be helpful to point out that the size of uncertainty intervals appears variable in Fig. 8 from point to point because the scale is logarithmic and the absolute uncertainty is constant. As mentioned above, type B uncertainty is attributed to the model in this comparison. Its magnitude is shown in Fig. 8 on the calculated curve as an uncertainty band within which analytical curves calculated with realistic input values are found. The values of thermophysical properties were chosen for each curve within the spread of values found in published literature.[7–9] Model adaptations discussed above to account for constriction and spreading resistances were included in the calculation. Residual questions on the validity of the adopted first approximation approach for the superposition of the two layers were not considered here, which may induce an underestimation of type B uncertainty at high frequencies, where the effect of the copper layer is felt.

The geometrical dimensions of the used device, a 34 pillars module (68 junctions), were measured wherever possible with a centesimal caliper. Results were conservatively taken to be (5.2 ± 0.02) mm for the total thickness and (0.9 ± 0.02) mm for the thickness of alumina ceramic insulator plates (L_2). The side width of the square cross section Bi_2Te_3 semiconductor pillars was measured to be (1.33 ± 0.02) mm and their length ($2L_0$) was assumed to be somewhere between 2.8 and 3.0 mm. The thickness (L_1) of copper electrical connections was consequently assumed to be between 0.2 and 0.3 mm. Better measurements could not be taken without disassembling the module.

The overall area filling factor $\xi = \xi_{0-1} \cdot \xi_{1-2}$ was measured to be 0.124 ± 0.02, while ξ_{0-1} was estimated by inspection to be between 0.4 and 0.6.

The Peltier module was driven by a sine wave current with peak value of 100 mA, yielding a 60 mA/mm² peak current density in the semiconductor pillars. Data points shown in Fig. 8 are normalized with respect to the low frequency ($\omega \approx \omega_p/10$) Seebeck voltage V_ε, which effectively makes them an experimental measurement of the quadrature component $^P\hat{\Theta}_0^\perp$ of the dimensionless temperature.

Dashed lines shown in Fig. 8 are included mainly for slope reference and are drawn a factor of $\sqrt{2}$ lower than asymptotes shown in Fig. 4 because they refer to a situation in which the temperature phase is $\pi/4$ from the injected current. As expected, the quadrature component vanishes at very low frequencies because at that end the heat flux is totally directed inward.

The good match obtained between measured values and analytical results shows that experimental data do not disagree with the theory and, therefore, stand to support it. More precise measurements might become strategic in the effort to turn the exposed theory into a tool usable to inquire into thermophysical properties of materials, but this goes beyond the scope of this paper.

NOMENCLATURE

A, B = dimensionless coefficients defined in the Appendix
e = thermal effusivity λ/α (W s$^{1/2}$ m^{-2} K^{-1})
f = frequency (Hz)
j = electric current density (A m^{-2})
L = layer thickness (m)
n = number of PN pillars of the Peltier module
p = Laplace transform variable
q = relative peak amplitude of heat fluxes
t = time (s)
V_ε = Seebeck voltage (V)
x = longitudinal coordinate (m)
X = dimensionless longitudinal coordinate

Greek symbols

α = thermal diffusivity (m^2 s^{-1})
ε = Seebeck coefficient (V/K)
ζ = aspect ratio
ϑ = temperature excess (K)
Θ = dimensionless temperature excess
κ = relative thermal diffusivity
λ = thermal conductivity (W pm^{-1} K^{-1})
Λ = relative thermal conductivity
ξ = area filling factor
Π = Peltier coefficient (V)
ρ_e = electrical resistivity (Ω m)
τ = dimensionless time
φ = phase for temperatures (rad)
Φ = heat flux density (W pm^{-2})
ψ = phase for heat fluxes (rad)
ω = angular frequency (rad s^{-1})
ω_0 = characteristic angular frequency of PN layer (rad s^{-1})
ω_p = angular frequency of the thermal pole (rad s^{-1})
Ω = relative frequency
Ω_c = relative corner frequency
Ω_k = relative knee frequency
Ω_p = relative frequency of the thermal pole

Superscripts

$-$ = identifies a Laplace transform
$\sim$ = identifies the oscillating component
$\wedge$ = identifies a balanced quantity
$\breve{}$ = identifies the lumped parameters model approximation
$+$ = refers to the positive x direction
$-$ = refers to the negative x direction
$\prime$ = indicates the first derivative
$\perp$ = identifies the quadrature component
P = identifies the peak value

Subscripts

0 = PN layer
1 = EC layer
2 = EI layer
i = generic layer

APPENDIX

Coefficients of Eq. (10)

$$A_0(X, \Omega) = \frac{M_1(N_2 - N_1) - M_2(N_2 + N_1)}{2(N_1^2 + N_2^2)\sqrt{\frac{\Omega}{2}}};$$

$$B_0(X, \Omega) = \frac{M_1(N_2 + N_1) + M_2(N_2 - N_1)}{2(N_1^2 + N_2^2)\sqrt{\frac{\Omega}{2}}}, \quad (A1)$$

where

$$M_1 = \sin\left[(1 - X)\sqrt{\frac{\Omega}{2}}\right]\cosh\left[(1 - X)\sqrt{\frac{\Omega}{2}}\right];$$

$$M_2 = \cos\left[(1 - X)\sqrt{\frac{\Omega}{2}}\right]\sinh\left[(1 - X)\sqrt{\frac{\Omega}{2}}\right]; \quad (A2)$$

$$N_1 = \sin\left(\sqrt{\frac{\Omega}{2}}\right)\sinh\left(\sqrt{\frac{\Omega}{2}}\right);$$

$$N_2 = \cos\left(\sqrt{\frac{\Omega}{2}}\right)\cosh\left(\sqrt{\frac{\Omega}{2}}\right). \quad (A3)$$

Coefficients of Eq. (16)

$$A_1(X, \Omega) = A_0(0, \Omega)\left[\frac{P_D Q_D + P_P Q_P}{Q_D^2 + Q_P^2}\right]$$
$$+ B_0(0, \Omega)\left[\frac{P_D Q_P - P_P Q_D}{Q_D^2 + Q_P^2}\right], \quad (A4)$$

$$B_1(X, \Omega) = B_0(0, \Omega)\left[\frac{P_D Q_D + P_P Q_P}{Q_D^2 + Q_P^2}\right]$$
$$- A_0(0, \Omega)\left[\frac{P_D Q_P - P_P Q_D}{Q_D^2 + Q_P^2}\right], \quad (A5)$$

$$A_2(X, \Omega) = A_0(0, \Omega)\left[\frac{T_a Q_D + T_b Q_P}{Q_D^2 + Q_P^2}\right]$$
$$+ B_0(0, \Omega)\left[\frac{T_a Q_P - T_b Q_D}{Q_D^2 + Q_P^2}\right], \quad (A6)$$

$$B_2(X, \Omega) = B_0(0, \Omega)\left[\frac{T_a Q_D + T_b Q_P}{Q_D^2 + Q_P^2}\right]$$
$$- A_0(0, \Omega)\left[\frac{T_a Q_P - T_b Q_D}{Q_D^2 + Q_P^2}\right], \quad (A7)$$

where

$$P_D = P_1 + P_3(E_2/E_1); \quad P_P = P_2 + P_4(E_2/E_1), \quad (A8)$$

$$Q_D = Q_1 + Q_5(E_2/E_1); \quad Q_P = Q_2 + Q_6(E_2/E_1), \quad (A9)$$

$$T_a = T_1 - T_2; \quad T_b = T_1 + T_2, \quad (A10)$$

with

$$P_1 = U_2(W_1 - W_2) + U_1(W_1 + W_2);$$

$$P_2 = U_2(W_1 + W_2) - U_1(W_1 - W_2);$$

$$P_3 = U_3(W_4 + W_3) - U_4(W_4 - W_3);$$

$$P_4 = U_3(W_4 - W_3) + U_4(W_4 + W_3); \qquad (A11)$$

$$Q_1 = V_2(W_1 - W_2) + V_1(W_1 + W_2); \qquad Q_5 = V_3(W_4 + W_3) - V_4(W_4 - W_3);$$

$$Q_2 = V_2(W_1 + W_2) - V_1(W_1 - W_2); \qquad Q_6 = V_3(W_4 - W_3) + V_4(W_4 + W_3);$$

$$Q_3 = V_1 W_3 - V_2 W_4; \qquad Q_7 = V_3 W_1 - V_4 W_2; \qquad\qquad (A12)$$

$$Q_4 = V_2 W_3 + V_1 W_4; \qquad Q_8 = V_3 W_2 + V_4 W_1.$$

$$U_1 = \sin\left[(X_1 + X)\sqrt{\frac{\Omega}{2\kappa_1}}\right]\sinh\left[(X_1 + X)\sqrt{\frac{\Omega}{2\kappa_1}}\right];$$

$$U_2 = \cos\left[(X_1 + X)\sqrt{\frac{\Omega}{2\kappa_1}}\right]\cosh\left[(X_1 + X)\sqrt{\frac{\Omega}{2\kappa_1}}\right];$$

$$U_3 = \sin\left[(X_1 + X)\sqrt{\frac{\Omega}{2\kappa_1}}\right]\cosh\left[(X_1 + X)\sqrt{\frac{\Omega}{2\kappa_1}}\right]; \qquad (A13)$$

$$V_1 = \sin\left(X_1\sqrt{\frac{\Omega}{2\kappa_1}}\right)\sinh\left(X_1\sqrt{\frac{\Omega}{2\kappa_1}}\right);$$

$$V_2 = \cos\left(X_1\sqrt{\frac{\Omega}{2\kappa_1}}\right)\cosh\left(X_1\sqrt{\frac{\Omega}{2\kappa_1}}\right);$$

$$V_3 = \sin\left(X_1\sqrt{\frac{\Omega}{2\kappa_1}}\right)\cosh\left(X_1\sqrt{\frac{\Omega}{2\kappa_1}}\right); \qquad (A14)$$

$$V_4 = \cos\left(X_1\sqrt{\frac{\Omega}{2\kappa_1}}\right)\sinh\left(X_1\sqrt{\frac{\Omega}{2\kappa_1}}\right).$$

$$W_1 = \sin\left[(X_2 - X_1)\sqrt{\frac{\Omega}{2\kappa_2}}\right]\sinh\left[(X_2 - X_1)\sqrt{\frac{\Omega}{2\kappa_2}}\right];$$

$$W_2 = \cos\left[(X_2 - X_1)\sqrt{\frac{\Omega}{2\kappa_2}}\right]\cosh\left[(X_2 - X_1)\sqrt{\frac{\Omega}{2\kappa_2}}\right];$$

$$W_3 = \sin\left[(X_2 - X_1)\sqrt{\frac{\Omega}{2\kappa_2}}\right]\cosh\left[(X_2 - X_1)\sqrt{\frac{\Omega}{2\kappa_2}}\right];$$

$$W_4 = \cos\left[(X_2 - X_1)\sqrt{\frac{\Omega}{2\kappa_2}}\right]\sinh\left[(X_2 - X_1)\sqrt{\frac{\Omega}{2\kappa_2}}\right]. \qquad (A15)$$

$$T_1 = \sin\left[(X_2 + X)\sqrt{\frac{\Omega}{2\kappa_2}}\right]\sinh\left[(X_2 + X)\sqrt{\frac{\Omega}{2\kappa_2}}\right];$$

$$T_2 = \cos\left[(X_2 + X)\sqrt{\frac{\Omega}{2\kappa_2}}\right]\cosh\left[(X_2 + X)\sqrt{\frac{\Omega}{2\kappa_2}}\right]. \qquad (A16)$$

Coefficients of Eqs. (17) and (18)

$$A_1'(0, \Omega) = \left.\frac{\partial A_1(X, \Omega)}{\partial X}\right|_{X=0}$$

$$= \sqrt{\frac{\Omega}{2\kappa_1}}\left\{A_0(0, \Omega)\left[\frac{Q_a Q_D - Q_b Q_P}{Q_D^2 + Q_P^2}\right]\right.$$

$$\left. + B_0(0, \Omega)\left[\frac{Q_a Q_P + Q_b Q_D}{Q_D^2 + Q_P^2}\right]\right\}, \qquad (A17)$$

$$B_1'(0, \Omega) = \left.\frac{\partial B_1(X, \Omega)}{\partial X}\right|_{X=0}$$

$$= \sqrt{\frac{\Omega}{2\kappa_1}}\left\{B_0(0, \Omega)\left[\frac{Q_a Q_D - Q_b Q_P}{Q_D^2 + Q_P^2}\right]\right.$$

$$\left. - A_0(0, \Omega)\left[\frac{Q_a Q_P + Q_b Q_D}{Q_D^2 + Q_P^2}\right]\right\}, \qquad (A18)$$

where

$$Q_a = 2[Q_8 + Q_4(E_2/E_1)]; \quad Q_b = 2[Q_7 + Q_3(E_2/E_1)].$$
$$\qquad (A19)$$

Coefficients of Eq. (20) $\forall\, i = 0, 1, 2$

$$\hat{A}_i(X, \Omega) = A_i(X, \Omega)\sigma_a - B_i(X, \Omega)\sigma_b, \qquad (A20)$$

$$\hat{B}_i(X, \Omega) = B_i(X, \Omega)\sigma_a + A_i(X, \Omega)\sigma_b, \qquad (A21)$$

where

$$\sigma_a = \frac{1 + \Lambda_1 B_1'(0, \Omega)}{[\Lambda_1 A_1'(0, \Omega)]^2 + [1 + \Lambda_1 B_1'(0, \Omega)]^2},$$

$$\sigma_b = \frac{\Lambda_1 A_1'(0, \Omega)}{[\Lambda_1 A_1'(0, \Omega)]^2 + [1 + \Lambda_1 B_1'(0, \Omega)]^2} \qquad (A22)$$

[1] B. J. Huang and C. L. Duang, Int. J. Refrig. **23**, 197 (2000).
[2] S. Lineykin and S. Ben-Yaakov, IEEE Power Electron. Lett. **3**(2), 63 (2005).
[3] H. S. Carslaw and J. C. Jaeger, *Conduction of Heat in Solids* (Oxford University Press, London, 1959), pp. 301–319.

[4]H. S. Carslaw and J. C. Jaeger, *Operational Methods in Applied Mathematics* (Dover, London, 1963), pp. 72–80.

[5]S. Lee, S. Song, and K. P. Moran, in Proceedings of the 4th ASME/JSME Thermal Engineering Joint Conference, Vol. 4, Maui, HI, p. 201 1995.

[6]see for example: R. A. Witte, *Electronic Test Instruments* (Prentice Hall, New York, 2002), pp. 167–170.

[7]N. P. Bansal and D. Zhu, NASA/TM—2003-212896, 2003.

[8]N. P. Gorbachuk, A. S. Bolgar, V. R. Sidorko, and L. V. Goncharuk, Powder Metall. Met. Ceram. **43**(5–6), 285 (2004).

[9]M. Takiishi, S. Tanaka, K. Miyazaki, and H. Tsukamoto, Proceeding of 27th Japan Symposium on Thermophysical Properties, Kyoto, p. 24, 2006.